IEEE Access
Multidisciplinary | Rapid Review | Open Access Journal

Received 2 July 2023, accepted 22 July 2023, date of publication 27 July 2023, date of current version 7 August 2023.

Digital Object Identifier 10.1109/ACCESS.2023.3299498

RESEARCH ARTICLE

Design, Analysis and Experiments of a High-Speed Water Hovering Amphibious Robot: AmphiSTAR

AVI COHEN AND DAVID ZARROUK
Department of Mechanical Engineering, Ben-Gurion University of the Negev, Be'er Sheva 84105, Israel

Corresponding authors: Avi Cohen (avi5@post.bgu.ac.il) and David Zarrouk (zadavid@bgu.ac.il)

This work was supported in part by the Pearlstone Center for Aeronautical Studies; in part by the Helmsley Charitable Trust through the Agricultural, Biological and Cognitive Robotics Initiative at the Ben-Gurion University of the Negev; and in part by the Marcus Endowment Fund at the Ben-Gurion University of the Negev.

ABSTRACT The development, modeling, and performance of AmphiSTAR, a novel high-speed amphibious robot, are detailed in this paper. The robot is palm-sized and fitted with propellers at its bottom, enabling it to crawl on the ground and hover on the water at high speeds. The design of the AmphiSTAR is inspired by two members of the animal kingdom - the cockroach's sprawling mechanism and the Basilisk lizard's ability to hover on the water at high speeds. We developed a relatively simple physical model of the lift force as a function of the size of the propeller, its submersion level, and rotational speed. We built an experimental setup to validate the results, and the experimental results are consistent with the analytical model. The robot can crawl at 3.6 m/s (13.6 bodylengths/s) and hover continuously on water surfaces at 1.5 m/s (5.6 bodylengths/s) speeds, making it the fastest amphibious robot. Its elevation on the water surface reduces friction, and its high-speed motors provide forward thrust, enabling it to move at high speeds. Additionally, it can swim by rotating its propellers while floating at low speeds and transition from swimming to crawling (see video).

INDEX TERMS Amphibious robot, crawling robot, design, water hovering.

I. INTRODUCTION

In recent years, multiple crawling robots [1], [2], [3], [4], [5], [6], [7], [8] were developed. However, they were primarily designed for crawling over dry land [8], [9], [10], [11], [12] but cannot propel themselves in aquatic environments or in the presence of water or mud (during floods, for example), which can cause sliding or wet their electronics. To address this limitation, miniature amphibious robots have been developed to respond to the challenges involved in search and rescue missions in flood zones, as well as for agricultural applications, cave exploration, and sewage maintenance. Floyd and Sitti [13] developed an experimental legged robot to analyze the dynamics of the Basilisk lizard [14]. Their results suggest that a legged robot running on the water cannot weigh more than a few grams, which implies that carrying batteries and cameras would be impossible. Robots must be even lighter if they rely on water surface tension to float and move [15], [16], [17]. Chen et al. considered beaver-like swimming [18], [19]. Other legged robots [20], [21] proved a certain level of amphibious capabilities at low speeds but relied on tethers.

Larger robots achieved better swimming and crawling performance. Undulating snake-like [22], and salamander-like [23] robots were reported to reach top speeds of up to 0.3 m/s and 0.5 m/s in water, respectively. The salamander was also able to crawl at 0.5 m/s on land. The minimally actuated Velox reached a swimming speed of 0.5 m/s but only traveled a few cm/s on land, whereas the SAW robot [24] reached speeds of up to 50 cm/s on land but only 6 cm/s in water.

In a different approach, the legged AQUA robot [25] uses its legs to crawl on land and as fins for swimming on the water's surface and underwater. The AQUA robot has a reported underwater speed of 1 m/s. Although it is similar in design to the RHex, its fin-like legs (as opposed to a C- shape)

The associate editor coordinating the review of this manuscript and approving it for publication was Jingang Jiang.

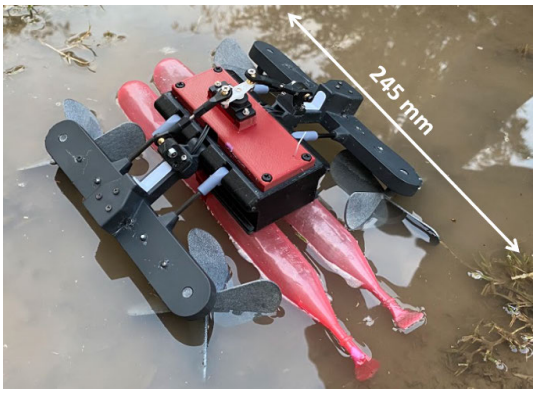

FIGURE 1. The AmphiSTAR is a newly developed STAR robot fitted with a sprawling mechanism and four propellers at its bottom. The two propellers at each side are actuated using a single brushless motor. The robot can crawl over the ground or swim and hover over water.

would likely substantially reduce its speed and stability on land (a supposition since its land speed is not reported in the literature).

While multiple research groups have presented partially submerged propellers (or surface-piercing propellers [26]), these propellers all rely on horizontal axes to produce horizontal thrust, where each blade is submerged for part of the revolution. These types of propellers are considered to be the most fuel-efficient propulsive device for high-speed vessels [27]. The main difficulty in modeling arises from the unknown physical behavior of the flow in the highly turbulent regime along the propeller. Yarri and Ghassemi [28] presented an analysis of the flow behavior of partially submerged propellers whose axes are horizontal. They implemented CFD (computational fluid dynamics) based on RANS (Reynolds averaged Navier Stokes equation) methods to generate simulated results and compared them to experimental data. Palik [29] investigated the performance of a partially submerged propeller and also used RANS with a Bollard condition, i.e., the inflow velocity was zero. They conducted their research on the partially submerged horizontal vertically oriented propellers and reported good consistency between the models and the experiments. However, these models involved complex flow theory [26] and [30].

In a previous conference, we presented an amphibious STAR robot (AmphiSTAR see Fig. 1) [31] based on our STAR robot family [5], [32] and conducted multiple experiments to evaluate its speed and performance. The AmphiSTAR can drive on land at 3.6 m/s (13.6 bodylengths/s) and hover over water surfaces at 1.5 m/s (5.6 bodylengths/s). To the best of our knowledge and according to the comparisons presented in [33] and [34] on amphibious robots, the AmphiSTAR possesses the fastest advancement on land and water.

Building on our previous work, we revisit our modeling and develop in this paper a theoretical model of the lift force as a function of the rotational speed of partially submerged propellers-like wheels (which we refer to as propellers in the paper) whose axes are vertical. We determined the relation between the main parameters that dictate the robot's behavior, such as the size of the propellers, the robot's weight, and the speed of the propellers.

We found that the displaced water volume is approximated as the height of the displaced water multiplied by the surface area of the propellers, implying that the robot can be scaled up with similar performance. We also developed experimental setups to validate our theoretical results for different parameter values and cases and estimate the thrust and lift forces that the robot can generate. The robot is intrinsically stable on the water even at high speeds.

This paper is organized as follows. We present the mechanical design of the AmphiSTAR and its components in Section II. The dynamic driving model of the robot hovering over the water and its stability are presented in Section III. The results of the force and torque experiments are in Section IV. Finally, experiments demonstrating the robot crawling over the ground, swimming, and hovering on the water are presented in Section V.

II. DESIGN AND MANUFACTURING

AmphiSTAR is designed as a lightweight all-terrain robot capable of changing its sprawl configuration inspired by cockroaches, swimming, and hovering over the water inspired by the basilisk lizard (see Fig 3). Given that our experiments showed that the lift force is nearly 300-320 grams at maximum speed, we limited the robot's weight to 250 grams to ensure it can lift itself above water level when rotating its propellers at high speeds. The length and maximum width of the robot are 245 mm and 260 mm, respectively. Its total weight is 246 grams, composed of the mechanical components weighing 149 grams, the battery weighing 43 grams, and its electronic components (receiver, controller, ESC, servo, and brushless motors) weighing 54 grams. The robot characteristics, and the weight of its parts are summarized in Table 1.

TABLE 1. Robot characteristics and part weights.

Robot Characteristics		Mechanical parts [g]		Electronics [g]	
Robot length	245 mm	Main body	37	Motor	11 × 2
Robot width	260 mm	Cover body	10	ESC (2 in 1)	5
Propeller diameter	90 mm	Propeller	7 × 4	Servo	23
Total mass	246 g	Arm	19 × 2	Receiver	4
Max ground speed	3.5 m/s	Gear	0.8 × 15	Controller	5
Max water speed	1.5 m/s	Push rod	8 × 2	Battery	43

A. ROBOT DESIGN

The AmphiSTAR (see Fig. 2) is composed of a main rigid body that houses the controller and receiver and the servo motor, which actuates the sprawl of the robot. The robot has two arms that hold the motor housing and propellers. A single brushless motor actuates the two propellers on each side.

The sprawl mechanism actuates two arms that can tilt symmetrically relative to its central body. As a result, while the propellers rotate at the same speed, the side forces cancel

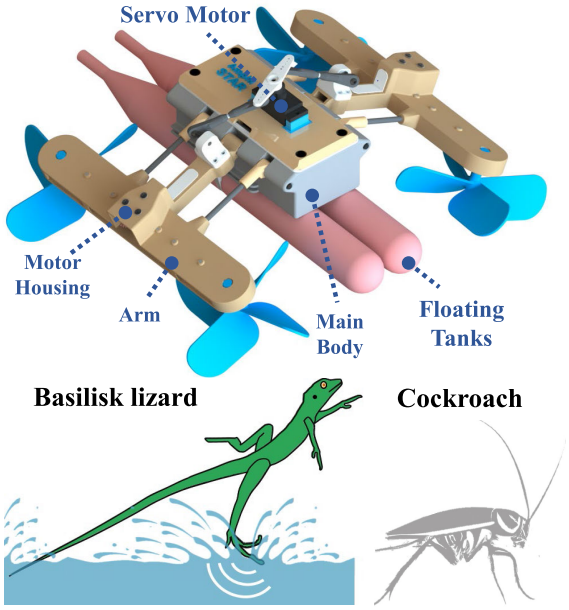

FIGURE 2. (Top) The mechanical design of the AmphiSTAR robot and its main components. The robot is driven by two brushless motors which actuate its propellers, whereas a servo motor fixed to the main body controls its sprawl angle. At its bottom, the robot can be fitted with optional floats that increase its survivability in case of water leaking. (Bottom) Basilisk lizard and cockroach.

out. However, they still generate vertical forces to lift the robot upwards and thrust forces to advance (see Fig. 3). Additionally, air tanks are positioned at the robot's bottom. These air tanks are made of plastic bags used in the food industry and supply buoyancy to keep the robot afloat at low speeds and safeguard against sinking in case of lost communication or malfunctions in the motors or controllers.

1) THE SPRAWLING MECHANISM

Similar to the previous STAR robots, we define the sprawl angle γ as the relative angle between the arms which hold the motors and propellers to the main body. A zero sprawl occurs when the arms are parallel to the body, and a positive sprawl occurs when the arms are rotated downwards.

The sprawl mechanism is kinematically a three-dimensional four-bar mechanism (two identical mechanisms on each side to ensure symmetry). The sprawl is actuated using a servo motor that rotates a small arm. A push rod is attached to the servo motor's arm tip with spherical joints. As the servo rotates its arm, it pulls or pushes the arms of the robot to fix their sprawl at the desired angle. More on the design of the sprawl mechanism and the forces needed to actuate it can be found in our previous work [32]. The sprawl angle in this design can be varied in the range of 0 to 30 degrees, as shown in Fig. 3.

2) THE ARMS, MOTOR HOUSING AND GEAR BOXES

A single motor powers the propellers on each side. A gear ratio of 1:16.7 is used to reduce the speed of the propellers and increase the torque. The torque is transmitted from the motor to the propellers via 4 consecutive spur gears. The main body which holds the electronics (controller and battery) is waterproof to ensure that the electronics do not get wet. However, the motor housing is not, and the brushless motors can function in water.

3) PROPELLERS

The custom-made propellers (two on each side) have four blades each. The propellers on the right and left sides of the robot have opposite pitches, so they both produce lift forces when they rotate in opposite directions. The 3D printed custom designed in preliminary experiments to increase their reliability to withstand the ground impacts and water pressure. More research should be made to optimize their design for water surfaces. Note that since water does not flow on both sides of the propellers, a hydrofoil shape will not have a significant effect on the lift. Therefore, our main concern is that the propellers will have a large working volume and be effective for ground locomotion over dirt, mud, stones, and grass.

Their diameter is 9 cm, their height is 2 cm, and their blade thickness is 1.5 mm. Their blade angle varies, ranging from 40 degrees at the center to 65 degrees on the external diameter. The shallower blade angle at the center allows for increased strength against breaking and bending. While increasing the diameter of the propellers would increase their lift forces, they must still be distanced to reduce their interference (which produces opposing/resisting flows). The distance between the centers of the propellers was fixed at two diameters, and the distance between their tips is nearly a single diameter.

B. ACTUATION AND CONTROL

Two brushless motors rotate the propellers (one at each side) while a servo motor actuates the sprawl mechanism in the 0-30 degrees range. The brushless motors can generate a torque of 0.4 Ncm and reach speeds of more than 30,000 RPM (2900 RPM/V) at 11.1 Volts. (Experiments on the torque and speed are presented in Section IV). The servo motor (HD-1810MG) has a rotational range of 145 degrees, weighs 16 grams, and produces a torque of 0.31 Nm. The controller (HGLRC F4.V2, which has multiple configurations enabling it to drive vehicles or fly drones) ensures the simple control of the robot using a simple joystick. The controller has built-in ESC (electric speed controllers) drivers and gyroscope sensors. We used BetaFlight configurator software to program the controller. The robot has intrinsic stability in the roll and pitch directions (see Section III-C and IV-E), hence, the control was disabled in these two directions (zero gains). We used a differential steering PID control in the yaw direction with no feed-forward (P=80, I=5, D=60).

C. MANUFACTURING

Most of the mechanical parts of the AmphiSTAR are manufactured using in-house 3D printing. We used a Form 2 printer (SLA), whose accuracy is roughly 0.1 mm for the arms and

small components, and an Ultimaker 5 printer (Fuse Deposition Modeling - PLA), whose accuracy is roughly 0.2mm, for the main body. We invested considerable effort in simplifying the design of the robot and reducing its weight to increase its speed while reducing its power consumption and ensuring it can hover on water.

III. ANALYTICAL MODELING

A. KINEMATIC ANALYSIS OF CRAWLING

On the ground, the propellers behave similarly to wheels with an effective radius $R_{eff}(\gamma)$, which is a function of the sprawl angle. The effective radius ranges from 33.4 cm to 37.5 cm, respectively, for the minimum sprawl angle, which allows crawling (13 degrees), to the maximum sprawl of 30 degrees.

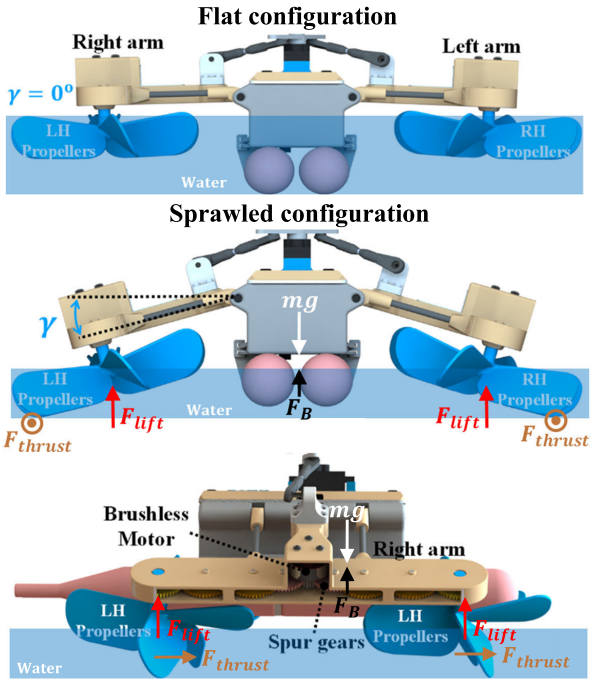

FIGURE 3. The sprawl mechanism, actuated using a servo motor, has a range of 30 degrees. The torque of the motors is transferred to each propeller using 4 consecutive gears with a gear reduction ratio of 1:16.7. Right-hand (RH) propellers are attached to the left arm, and left-hand (LH) propellers are to the left arm.

Based on our design, the effective radius of the propeller is (as defined in Fig. 4):

$$R_{eff}(\gamma) = r_{tip} \sin\gamma + r_{center} \tag{1}$$

where r_{tip} and r_{center} are equal to 15 mm and 30 mm, respectively.

Our experiments (see Section V-A) show that the ground crawling speed is slightly smaller than the product of the rotational speed of the propellers α times the effective radius R_{eff}, which implies that there is very little sliding during locomotion:

$$v_{ground} \leq \alpha \cdot R_{eff}(\gamma) \tag{2}$$

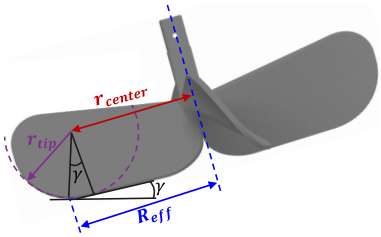

FIGURE 4. The geometry of the propeller. The propeller has rounded ends to decrease contact forces with the ground.

The absolute values of the forces acting on one side of the arms, in the normal and fore-aft directions relative to the robot's main body, are denoted by N, and F_f (see Fig. 5). The torque required to operate the propellers when moving on an inclined surface with an angle φ is T_{motor}. Given the symmetry of the robot, the analysis is performed on a single side that holds half of the weight (and each propeller a quarter of the total weight). The torques that must be provided by the motors when climbing an inclined surface are approximated as follows:

$$T_{motor} \approx R_{eff}(\gamma) \cdot \frac{m}{2} \cdot g \sin\varphi \tag{3}$$

The approximation is due to the fact that along the ground locomotion, the propellers will combine both rolling on the ground and sliding sideways. The design of the propellers is atypical to a standard design, which has a constant overall pitch and varying blade angles along the blade span. Given that in our robot, the tips of the propellers contact the ground, it was imperative to have a high pitch angle at the tip to avoid sliding and producing thrust in the water.

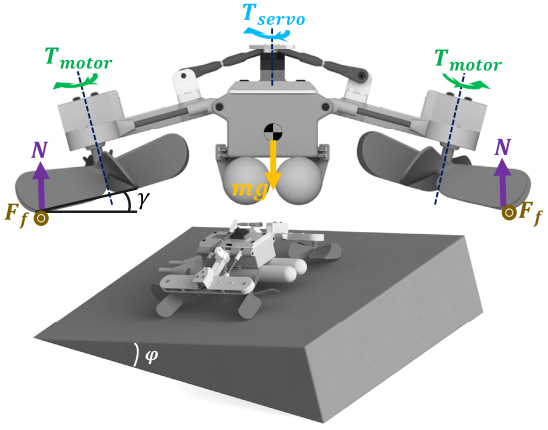

FIGURE 5. (Top) The forces and torques are acting on the robot during driving. (Bottom) Illustration of the robot moving over an inclined surface.

B. BACKGROUND ON LIFT AND BUOYANCY

In general, quadcopters of the size of our robot produce lift forces by rotating their propellers at more than 5000 RPM. In this type of robot, the propellers in contact with the water rotate in a range of 100-1000 RPM, which is insufficient to

produce airlift for flying (i.e. if it increases its propellers' speed by five fold, it becomes airborne). Therefore, the propellers' interaction with the water keeps the robot afloat. Given that the lift force is proportional to the density of the fluid and to the square of the rotational speed $F_{lift} = C_L \rho \alpha^2 R^4$ it is obvious that the water produces most of the lift given that its density is three orders of magnitude larger than the density of the air (ρ_w =997 kg/m^3 $\gg$ ρ_a =1.22 kg/m^3). This assumption remains correct even if only a small fraction (roughly 5%) of the propeller is submerged and the rest is in the air. Therefore, the analysis presented below focuses first on the lift caused by the water, and the effect of the airlift will be estimated afterward.

Two different forces keep the AmphiSTAR afloat [31] as presented in Fig. 6: buoyancy forces F_B and lift forces F_{lift}. In (A), the propellers are at rest or rotating at low speed, so the lift forces are negligible compared to the buoyancy forces F_B, which are equal to its weight mg. In (B), the propellers rotating at high speed produce lift forces that elevate the robot relative to the water level, reducing the buoyancy force's magnitude F_B. As shown below, the lift forces F_{lift} increase as a function of the rotational speed after reaching a maximum value.

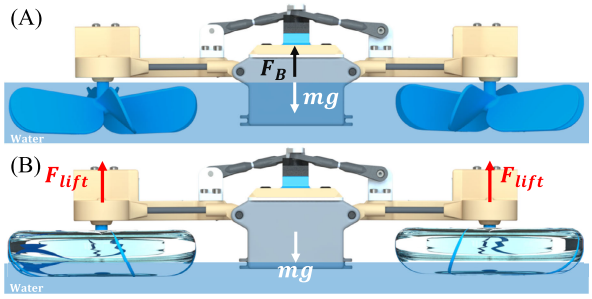

FIGURE 6. (A) The robot floating on the water. Its weight is equal to the buoyancy forces. (B) the robot hovers over the water's surface by rotating its propellers. The impact of the propellers with the water displaces the water underneath them, creating vertical pressure (lift force). At high speeds, the lift force is sufficient to lift the robot.

C. HOVERING MODEL

We first detail the lift force produced by the propellers in the water. When the propellers start to rotate at a rotational speed α, they create thrust resulting in a lift force that acts on the robot. As a result of this force, the robot is lifted, and its depth of submerge, as well as the propeller's depth of submerge is reduced. As the propeller's depth of submerge (h_w in Fig. 7A) is reduced the thrust force decreases too until, eventually, equilibrium with the robot weight is achieved. We found that as the rotational speed increases, the propellers displace a larger water depth beneath them, which creates pressure that lifts the robot upwards. Therefore, along with the actuation of the robot, the propellers are only partially submerged in water, and the effective part of the propeller is substantially smaller at high speeds.

We assume that the propellers' axes are rigidly fixed and do not move with the rotation of the propellers. Using blade element theory, the propeller blade is divided into elements, and each element acts as a wing airfoil (see Fig. 7). The circumferential velocity of each element v is a function of the rotational speed and the distance from the axis alone $v = \alpha r$. Using the lift coefficient definition for wing airfoil $C_l = 2f_{lift}/\rho v^2 c$, where f_{lift} is the lift force per unit length, we can calculate the element lift force contribution:

$$df_{lift}(r) = \frac{1}{2}\rho_w \cdot v^2(r) \cdot c_w(r, \alpha) \cdot C_l(r) \cdot dr \tag{4}$$

where c_w is the chord length projection on the horizontal surface (see Fig. 7C). In a general propeller, the chord length c_w is a function of the distance from the rotation axis r alone. However, in this case, given that the propellers have a uniform shape, the effective chord length which is in contact with the water is a function of the rotational speed (given that the water level drops with the increase in speed). The total lift force that the propeller applies on the water is:

$$F_{lift} = N_b \int_{R_{root}}^{R} df_{lift}(r) \tag{5}$$

where R_{root} is the root radius of the propeller, N_b is the number of blades, and N_p is the number of active propellers. By integrating the lift force, with the assumption that c_w and C_l are independent of r and that R_{root} is very small compared to R, the lift force becomes:

$$F_{lift} = \frac{R^3}{6} \cdot N_b N_p \cdot \rho_w \cdot \alpha^2 \cdot c_w(\alpha) \cdot C_l(\alpha) \tag{6}$$

The chord length c_w can be expressed as a function of the water height h_w and the blade angle $\tan\theta = h_w/c_w = h_p/c$ (see Fig. 7C).

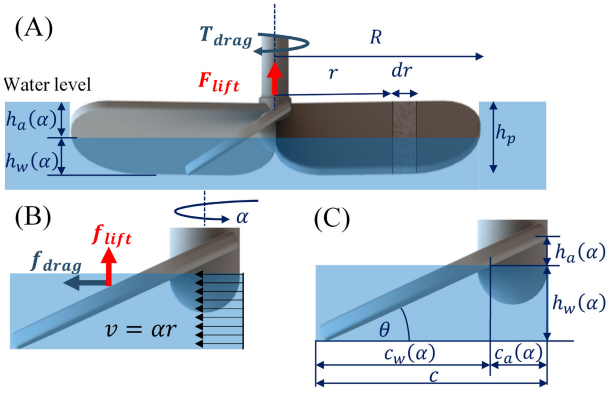

FIGURE 7. (A). The lift force F_{lift} and torque T_{drag} acting on the propeller whose height is h_p and its radius is R. As it rotates, the propeller applies vertical pressure, which displaces a water volume whose depth is h_a where h_w is the part of the propeller that remains plunged in the water. dr is the blade element at a distance r from the rotation axis. (B). The lift force f_{lift} and drag force f_{drag} (on a single blade) due to water velocity $v = \alpha r$. (C). Geometric definition of the blade. The blade angle is θ. The chord projection on the water's surface is c. The projection of the chord below the water level is c_w, whereas c_a is the projection of the part above the water level.

When inserting the blade angle θ into (6), the lift force becomes:

$$F_{lift} = \frac{R^3 \cdot N_b N_p \cdot \rho_w \cdot \alpha^2 \cdot h_w(\alpha) \cdot C_l}{6 \tan\theta} \tag{7}$$

Alternatively, the lift force can be calculated from the pressure difference according to Momentum Theory (or Archimedes' principle) as the weight of the water displaced by the propeller's rotation (described in [31]):

$$F_{lift} \approx N_p \rho_w g A \cdot h(\alpha) \tag{8}$$

where A is the disk area of the propeller, h_p its height, h_a is the height of water displaced by the propeller and is equal to $h_a(\alpha) = h_p = h_w(\alpha)$. By inserting the value of F_{lift} from (7) into (8), the height h_a can be represented as a function of the rotational speed:

$$h(\alpha) = \frac{h_p R^3 C_L \alpha^2}{R^3 C_L \alpha^2 + 6Ag\tan\theta} = \frac{k_1 h_p \alpha^2}{k_1 \alpha^2 + k_2} \tag{9}$$

where $k_1 = N_b R^3 C_l$, $k_2 = 6A\tan\theta$ and $C_L = N_b C_l$. According to this model, the lift increases linearly as a function of the number of propellers. Decreasing the number of propellers will require a higher speed to attain the same lift force and vice-versa.

D. ESTIMATING THE RATIO OF THE AIR LIFT TO WATER FORCES

Recall that the lift force is $F_{lift} = F^a_{lift} + F^w_{lift}$ is composed of the lift forces of the water and the lift force of the air. However, we assumed it was mostly created by contact with the water. Next, we estimated the ratio of each of the forces on the overall lift force. The height of the immersed portion of the propeller is h_w, whereas the height in the air is h_a for a constant blade angle.

The ratio of the length of the chord submerged in water and the air is proportional to the heights h_w and h_a: $h_w/h_a = c_w/c$. The general lift force can be written as:

$$F_{lift} = \frac{R^3}{6} \cdot N_b N_p \cdot (\rho_w c_w + \rho_a c_a) \cdot \alpha^2 \cdot C_l(\alpha) \tag{10}$$

The ratio of the airlift to the water lift $\beta = F^a_{lift}/F^w_{lift}$ is, therefore, proportional to $\rho_a c_a/\rho_w c_w$. Alternatively, $\beta = \rho_a c_a/\rho_w c_w$. at low speeds, the height h_a is very small and β is very small. At high speeds, h_a becomes larger than h_w, and the robot may even become airborne. However, for the working speeds of the robot in the range of 100 RPM to 1200 RPM the dynamics do not vary much and β remains small. For example, at 1000 RPM, based on (10), the ratio h_a/h_w was 20, and β was 2.5%. At 1500 RPM, which is beyond the robot's working range, the ratio β became 8%. However, given the large difference in densities, it remained small. Therefore, the assumption used at the beginning of the analysis is correct.

E. GENERAL TYPE OF PROPELLERS

In contrast to the previous model, which featured a uniform blade angle across all radii, the general type of propellers is characterized by varying blade angles at different radii. The lift force can also be calculated as a function of the water volume displaced by the propeller's rotation. In this case, the equation for extracting the height h_a for general propellers is:

$$\frac{h_w(\alpha)}{h_p} C_L \rho_w \alpha^2 \cdot R^4(h_a) \approx \rho_w g \int_V dV\,(R(h_a)) \tag{11}$$

By rearranging the equation and inserting $h_a = h_p - h_w$, we obtain:

$$\frac{(h_p - h_a(\alpha))}{h_p} C_L \alpha^2 \cdot R^4(h_a) \approx g\pi \int_0^{h_a} \left[R_2^2(h_a) - R_1^2(h_a)\right] dh_a \tag{12}$$

Equation (12) converges asymptotically to h_p, and the lift force becomes equal to the weight of the water, whose volume is the rotating volume of the propeller.

F. ROLL STABILITY

When the robot turns in the water, a centripetal force F_{cent} will act on its center, causing it to tilt around its roll axis. Interestingly, when both sides of the robot are partially submerged, the robot has intrinsic stability. Because as the robot tilts to one side, the lift force increases (linearly) on the lower side and decreases on the other side, producing a restoring moment in the roll direction $M_{restore}$:

$$M_{restore} = (F^L_{lift} - F^R_{lift})\frac{w}{2} \tag{13}$$

The indices L and R denote the left and right sides of the robot, respectively, and w is the distance between the centers of the two propellers (see Fig. 8). Assuming a constant rotation speed, and inserting (8) into (13), the height difference between the two sides becomes:

$$M_{restore} = (h^L - h^R) N_p \cdot \rho_w \cdot g \cdot A \frac{w}{2} \tag{14}$$

Assuming a small tilt angle λ (as demonstrated in the experiments), the restoring moment can be alternatively written as:

$$M_{restore} = N_p \cdot \rho_w \cdot g \cdot A \frac{w^2}{2} \sin\lambda \tag{15}$$

Alternatively, if a perturbation torque is applied in the roll direction, the tilt of the robot will be:

$$\lambda = \arcsin\left(\frac{N_p \cdot \rho_w \cdot g \cdot A \cdot w^2}{2M_{perturbation}}\right) \tag{16}$$

This shows that the restoration torque is proportional to the square of the distance w between the propeller and the sine of the tilt angle λ.

Assuming that the robot is turning at a radius $R_{turning}$ while hovering over the water at speed V_{robot}, a "centripetal" force will produce a tilting torque whose value is:

$$M_{cent} = m\frac{V^2_{robot}}{R_{turning}}\Delta d \tag{17}$$

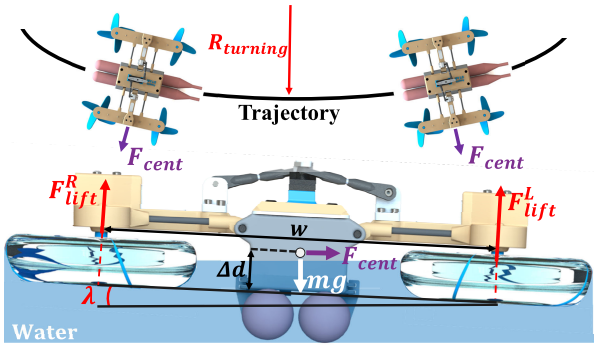

FIGURE 8. (Top) The robot turns at speed V_{robot} and a turning radius $R_{turning}$. (Bottom) The robot tilts to the left by a small angle λ due to the centripetal force F_{cent}.

where Δd is the height between the contact of the robot with the water and its COM as defined in Fig. 8. By equating the centripetal torque to the restoring torque, the tilting angle can be calculated using the following:

$$\lambda = \arcsin\left(\frac{2 \cdot m \cdot \Delta d \cdot {V_{robot}}^2}{N_p \cdot \rho_w \cdot g \cdot A \cdot w^2 \cdot R_{turning}}\right) \quad (18)$$

IV. EXPERIMENTS

The experiments in this section are to validate our theoretical expectations, measure the forces we are not capable of modeling and evaluate the robot's stability. In Section IV-A, the lift force is measured as a function of the propeller's speed and compared to theoretical expectations. Then using the propellers' speed, we estimated the airlift to water lift in Section III-D. In Section IV-C, we verified our model using the custom propellers we fitted our robot. Given that the model is too complex for sprawled configurations, we experimentally measured the lift and thrust forces of the robot for different sprawl angles. In Section IV-B, we measured the same thrust force for a more realistic scenario when the robot is floating on the water (i.e.) the propellers' depth is not constant in the water. Finally, given that the robot is highly dynamic, we evaluated its stability in the roll direction by implementing a disturbance and measuring how it affects its motion. We also simulated centripetal acceleration by inserting weights on the robot's side in Section IV-E.

The experimental system presented in Fig. 9A is composed of a motor house that rotates a propeller and a water tank. The motor house is held by a rigid arm attached to a 6 DOF Nano 25 force sensor whose accuracy is 0.01 N. Throughout the experiments, the rotational speed of the propellers was controlled using a Teensy 3.5 controller, and the rotation speed (using the encoder) and lift force were continuously measured and saved for post-processing. In the experiments, 5 propellers with different radii and blade angles (constant and variable) were used. One was identical to the one eventually used in the actual robot. Given the motor's KV (2900 RPM/Volt) and a gear ratio of 1:16.7 between the motor and the propeller, the propeller can theoretically reach a speed

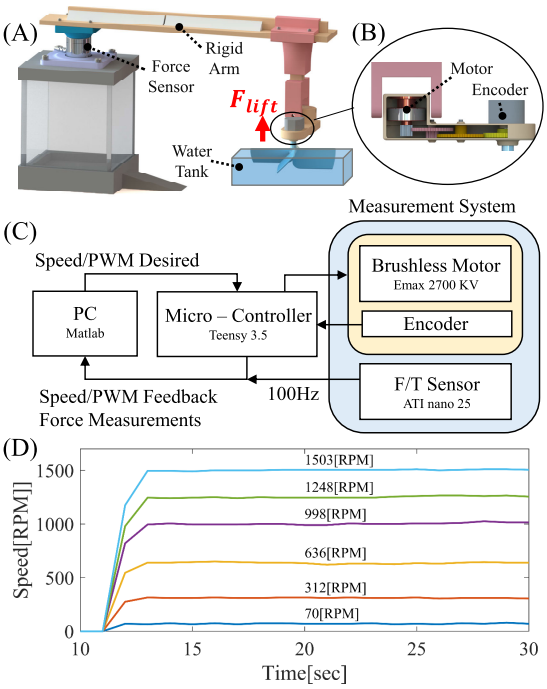

FIGURE 9. (A) The experimental system used to measure the lift forces as a function of the rotational speed and depth of the propeller. The experimental setup comprises a rigid arm that holds a brushless motor that rotates the propeller and an ATI NANO 25 force sensor. The speed of the propeller is controlled in a closed loop using a Teensy microcontroller and an encoder attached to the propeller. (B) The power transmission gearbox and the encoder. A gearbox with a ratio of 1/16.7 is used to increase the torque produced by the motor. The encoder is directly attached to the propeller and covered for protection from water droplets during the experiment. (C) Experimental scheme for the measurement system. The PC sends the desired PWM or rotational speed to the microcontroller, which controls the speed in a closed loop. The force sensor records the measured forces at 100 Hz. The output is saved and processed using MATLAB software. (D) The rotational speed of a single propeller as a function of time for different duty cycle inputs (PWM).

of 1900 RPM when powered by an 11 Volt input. However, the actual system's speed was limited to 1600 RPM, possibly due to friction losses. The output recorded speed was relatively smooth, and the maximum standard deviation of the speed was less than 13.8 RPM (less than 1% of the maximum measured speed - Fig. 9D). At the lowest limits, it was possible to run the propeller at nearly 50-60 RPM. Below that value, the rotational speed became unstable.

A. LIFT FORCE AS A FUNCTION OF THE ROTATIONAL SPEED

In this experiment, the lift forces were measured as a function of the rotational speed (in RPM). The propellers were fully plunged into the water until their tips were just below the surface. We assumed a visual error of $\pm$ 1mm in adjusting the water level. The experiment was run at different rotational speeds for two different propellers whose radius was 43 mm. Fig. 10 presents the lift forces in the range of 0 to 1500 RPM as measured by the Nano 25 force sensor.

The lift force initially increased similarly to a fully plunged propeller but then increased at a lower rate (almost linearly)

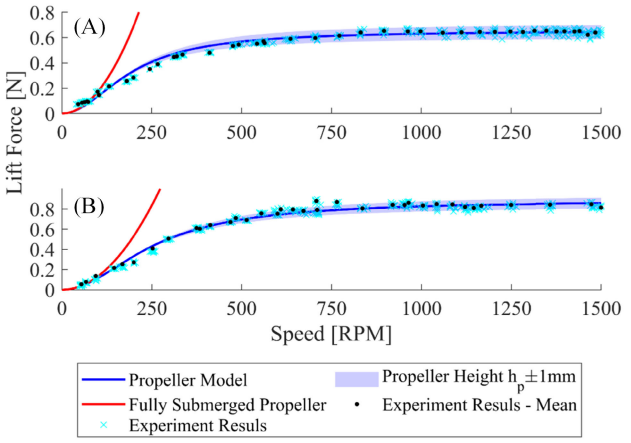

FIGURE 10. The lift force as a function of the rotational speed of the propeller for two blade angles, see Fig. 7. (A) blade angle of 30 degrees, (B) blade angle of 45 degrees. The red line represents the lift force the propeller will produce when fully submerged in the water, i.e., the propeller is acting as a classical propeller, and its lift force is proportional to the rotation speed squared. The blue line represents the propeller model, shown in equations (8) and (9). The purple area represents the uncertainty due to the limited accuracy in measuring the water level.

until the range of 400 RPM. Beyond that speed, the lift forces increased at a lower rate until converging to a maximum value of 0.64 N and 0.85 N for the 30 and 45 degrees blade angles. This result is identical to our theoretical predictions, which show that the force converges to the water weight of the rotation volume of the propeller as per equation (8). Note that at the beginning of the experiment, the water exerts buoyancy forces on the propellers before they start rotating. Therefore, the estimated weight of the portion of the propeller that went above the water level during the experiment was added to the measured lift force. The results were consistent with our theoretical expectations, and the average error was 2.4%.

B. GENERAL TYPE OF PROPELLERS

To validate that the theory was applicable to general propellers with varying blade angles and radii, we ran multiple experiments on propellers with different dimensions. The experiments included determining the forces as a function of the speed and the maximum forces that can be generated at 1000 RPM for different sizes and depths. To compare the experiments and the analytical results, we experimentally measured the lift coefficient C_L, using $C_L = F_{lift}/(\rho\alpha^2 D^4)$. By introducing the approximation that C_L is constant along the height h_a, the lift force becomes proportional to h_w/h_p (similar to the case where the blade angle was constant).

We printed three propellers, each with a different external radius R: (35 mm, 39 mm, and 45 mm). The three propellers were rotated at 1000 RPM (in the same experimental system as presented in Fig. 9A) at four different depths in 5 mm steps starting from 9 mm (nearly halfway through the water) to 14 mm, to 19 mm and finally 24 mm. At the largest depth, the propeller was fully plunged into the water. Throughout the experiment, the propellers were rotated at 1000 RPM with a closed loop control using the Teensy 3.5 controller while the forces were measured and saved at 100 Hz. At 1000 RPM, the height h_a as per equation (12) was expected to be 95% of the total height h_p of the propellers.

In order to compare the experimental results to the theoretical expectations, the rotating volume of each of the three propellers at the four different depths was calculated using Solidworks CAD (a total of 12 volumes). The measured forces and the comparison to the theoretical expectations are presented in Fig. 11 (four depths for each of the three propellers). The measured forces were slightly smaller than the theoretically estimated forces, and the average percentage error was 11.7%. This difference between the estimated and measured forces may have been due to water leakage into the work volume during the propeller rotation, which decreased its magnitude and hence, decreased the generated lift forces.

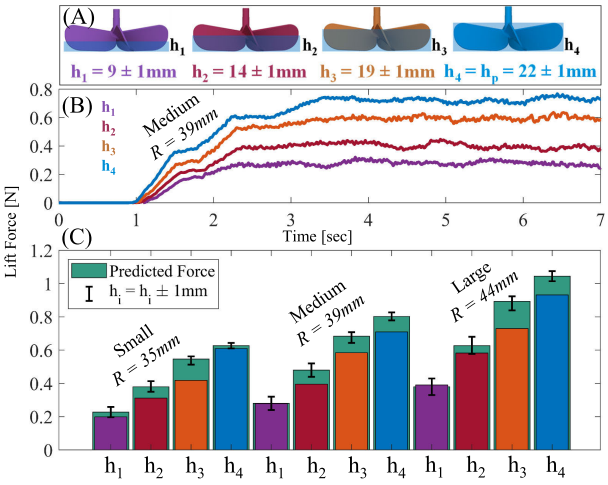

FIGURE 11. (A) The depth of the water in which the propellers were immersed ($h_1 = 9$, $h_2 = 14$, $h_3 = 19$, and $h_4 = 24$ mm). Three propellers with different radii were used ($R = 35$, 39, 44 mm). Measurement of the water level may involve an error of around 1 mm. (B) The lift forces as a function of time on the medium size propeller for four different depths (9, 14, 19, 24 mm). (C) A comparison of the theoretical to the experimental lift forces as a function of the depth of the propeller at 1000 RPM for three different sizes and four different depths. The error bar represents the predicted lift force with the expected error due to inaccuracies in water height measurement.

C. LIFT AND THRUST FORCES IN THE SPRAWLED CONFIGURATION

Since the robot can only advance in the sprawl configuration due to the pressure difference between the two sides of the propeller, we measured the thrust forces of the robot as a function of the rotational speed of the propellers when the sprawl angle was at 0, 10, 20 and 30 degrees.

The results, presented in Fig. 12, show that the lift force continued to increase until the range of 600 RPM (similarly to zero sprawl) and retained its value for higher speeds. Note that, as predicted by our model, the thrust forces for 20 degrees sprawl are twice large as the 10 degrees case. The increase between 20 to 30 degrees is 18% only (instead of $\sin(30°)/\sin(20°) = 46\%$). Probably since the propeller is

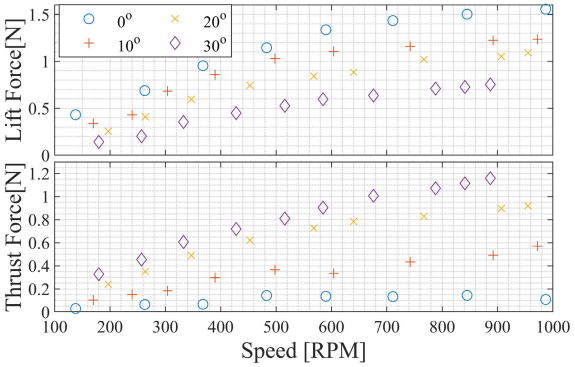

FIGURE 12. The lift and thrust forces for 0, 10, 20, and 30 degrees sprawl angles as a function of the rotation speed.

TABLE 2. The height of the robot and the thrust forces as a function of the rotational speed for different sprawl angles.

	Elevation [cm]			Thrust [N]		
Sprawl [deg]	10	20	30	10	20	30
∼100 rpm	0.6	0.4	0.4	0.11	0.1	0.13
∼300 rpm	1.0	1.0	0.9	0.3	0.4	0.53
∼500 rpm	1.2	1.5	1.5	0.43	0.65	0.71
∼700 rpm	1.2	1.7	1.9	0.45	0.75	0.88
∼900 rpm	1.2	1.8	2.1	0.45	0.77	1.1

becoming like a wheel. A low sprawl (a nearly flat configuration) can be used for traveling with payloads at low speeds, whereas a higher sprawl can be used to travel at higher speeds.

D. ROBOT ELEVATION AND THRUST FORCE DURING HOVERING

The robot was fixed to a 25 cm long beam attached to a rotational joint. The rotational joint was attached to a Nano 25 force sensor which measures the thrust force. When the robot was actuated, it could not advance but only lift its body relative to the water and tilt slightly upwards (pitch). At the beginning of the experiment, the robot was freely floating over the water using its buoyancy forces alone. For each of the three sprawl angles, the robot was actuated at five different speeds (100, 300, 500, 700, and 900 RPM). Each experiment was repeated twice, and the actuation of each speed lasted 10 seconds (see Fig. 13). The height of the robot was measured using the OptiTrack system. The elevation and thrust forces results are summarized in TABLE 2. At the maximum input speed, the lift force generated by the propellers elevated the robot by up to 2.1 cm at the maximum sprawl angle (30 degrees). At the lowest sprawl angle (10 degrees), increasing the speed beyond 500 RPM did not result in higher thrust. By contrast, the force continued to increase with the rotational speed at a 30 degrees sprawl until reaching a maximum thrust of 1.1 N at 900 RPM. The thrust forces generated by the propellers when they were fixed (Section D) versus when the robot was floating (this Section) show nearly identical results (Section D and Fig. 12)

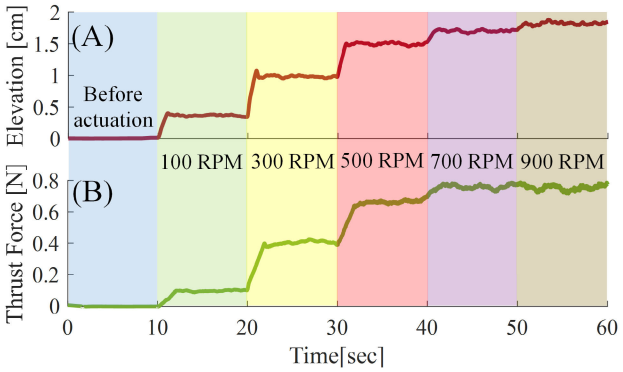

FIGURE 13. (A) The elevation of the robot due to the rotation of the propellers as a function of the rotational speed at 20 degrees sprawl. (B) The thrust force generated by the robot as a function of the rotational speed.

E. ROLL STABILITY

In this section, we report measurements of the restoring time in case of perturbations and the tilting angle of the robot in the roll direction in the presence of side forces (similar to centripetal force) and compare them to the theoretical predictions as presented in the equation (18). The robot was attached to a rotational axis with bearings preventing it from advancing but allowing it to rotate freely in the roll axis only. The propellers were completely submerged in the water at the beginning of the experiment (see Fig. 14 and video).

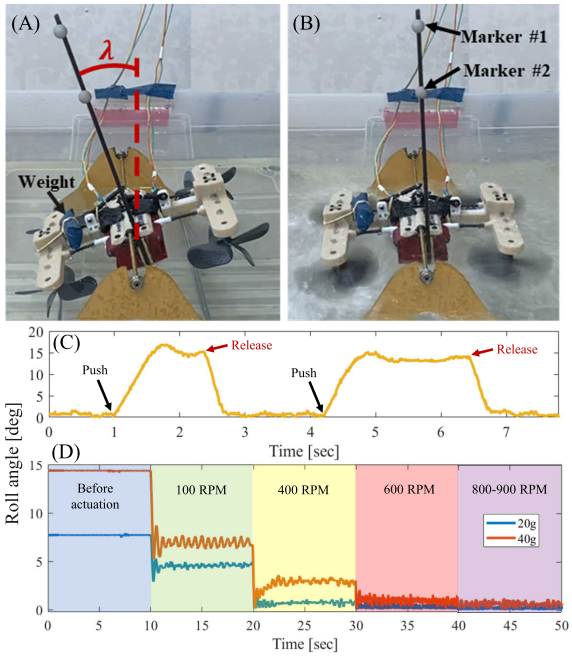

FIGURE 14. (A) The robot is tilted by a weight placed on its side. (B) the robot was restoring its horizontal position after actuating the propellers. (C) The robot recovered from an external perturbation of 15 degrees in only 0.5 seconds. (D) Experiments were performed to measure the robot's tilt from a mass placed on its side as a function of speed (see video).

Two reflective markers, placed on a rod attached vertically to the robot, were used to measure the roll orientation with the OptiTrack system. In the first experiment, the propellers were actuated at 600-700 RPM, and an external perturbation of 15 degrees was applied to the robot (see Fig. 14C). The robot recovered its horizontal direction in only 0.5 seconds. In the second experiment, two weights (20 and 40 grams) were placed on the robot's side to produce a continuous torque that mimicked the centripetal torque M_{cent} that acts on the robot while it rotates. The rotation speed was increased in four steps by changing the input PWM until reaching a speed of 800-900 RPM. The resulting deviations at top speed were 0.27 and 0.63 degrees, respectively, for 20 and 40 grams. These results are very close to our predicted tilt in equation (18) (0.36 degrees and 0.72 degrees). Given that the robot's top speed is 1.5 m/s and Δd =2 cm, the largest weight (40 grams) produced a torque that is comparable to when the robot turns at its top speed at a turning radius of less than 0.46 m, which is substantially smaller than what the robot achieved during the experiments.

V. ROBOT PERFORMANCE

In this section, we tested the AmphiSTAR as it crawled over various surfaces in swimming and hovering on water modes. All the experiments presented below were controlled by a human operator (combined with the onboard controller). The robot demonstrated high reliability, successfully and repeatedly performing the experiments without requiring maintenance during filming (excluding battery replacement). The robot has a 0.4 Ah battery and draws 5 A at its top speed (1000 RPM and 1.5 m/s on water). Based on this energy consumption, the robot can travel nearly 450 m in the water at a top speed.

A. CRAWLING EXPERIMENTS

1) IN-LAB CRAWLING EXPERIMENTS

We first tested the robot in the laboratory over carpet surfaces. The robot was turned clockwise and counterclockwise at a turning radius of nearly 0.2 m. The robot was then successfully driven over an incline.

The robot was also run at high speeds over a carpet at a sprawl angle of 20 degrees while its location was recorded using the OptiTrack system at 120 Hz. The effective radius $R_{eff}(20°)$ at this sprawl angle was 3.4 cm. Because there are no encoders on the robot, we attached reflective markers that rotate together with the propellers to measure the actuation rotational speed of the propellers and compared it to the linear speed. In total, 26 experiments at speeds ranging from 1.4 to 1.9 m/s were performed as the robot was driven in a straight line (see Fig. 15A).

To validate our assumption that the propellers behave like wheels, we compared the robot's linear speed to the propellers' rotational speed times the effective radius R_{eff} as in equation (2). The average propeller speed was only 3.6% higher than the linear speed of the robot, with a standard deviation of 7.5% (see Fig. 15C). These results show that the four-blade propellers behave nearly like regular wheels in terms of speed but would probably consume much more energy while traveling.

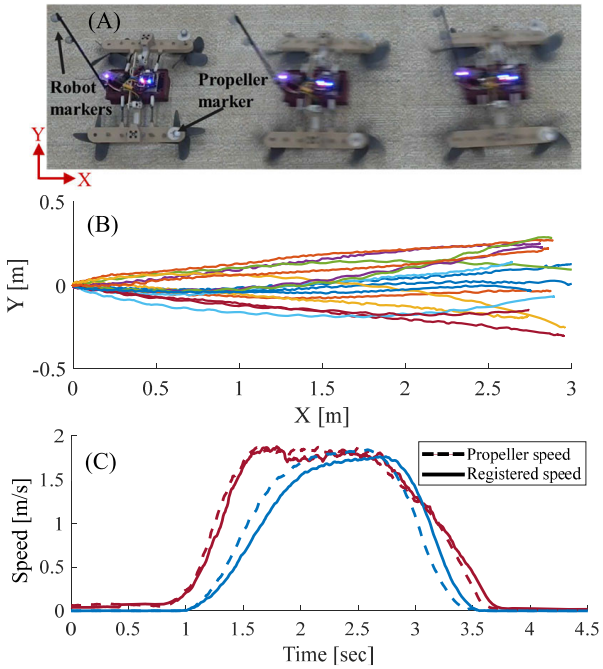

FIGURE 15. (A) The AmphiSTAR driven in the lab at 1.8 m/s was filmed at 240 fps (see video). (B) The trajectories of the robot as recorded using OptiTrack. (C) A comparison of the recorded speed using the OptiTrack to the propeller speed. Two experiments, dashed lines represent the propellers' speed and solid lines represent the robot speed.

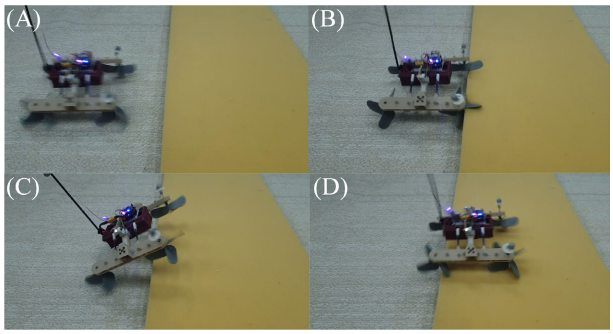

FIGURE 16. The AmphiSTAR climbing over a 3.8 cm step obstacle at a sprawl of 30 degrees.

2) CLIMBING OVER OBSTACLES

We drove the robot towards a step obstacle to verify the maximum height the robot could climb. The robot, at 30 degrees sprawl, successfully climbed over a maximum height of 3.8 cm high obstacle (see Fig. 16 and video).

B. SWIMMING AND RUNNING ON WATER EXPERIMENTS

1) IN-LAB SWIMMING EXPERIMENTS

In the first experiment, the robot was placed on an incline and driven toward a small pool of water. The robot was actuated at

low speeds so its propellers could act as fins and its air tanks provided the floating forces (see video). The robot crawled slowly over the ramp towards the water, swam forward as its propellers acted as fins, then rotated and returned to the ramp to climb back onto the ramp (see video). In the second experiment, also presented in the video, the AmphiSTAR was driven until it fell into the water. At this point, the propellers were actuated at high speed. The lift forces elevated its body above the water, and the robot ran on the water and then climbed over the ramp at high speed.

2) OUTDOOR WATER HOVERING EXPERIMENTS

After successfully testing the robot in the small pool, the robot was taken outdoors to a large puddle with muddy edges measuring up to 20 cm in depth and into a small artificial pond (see Fig. 17 and video). The robot easily crawled over the mud and ran on the water at estimated speeds of up to 1.5 m/s. The robot crossed (18 m) multiple times in the artificial pond while hovering on the water in windy conditions against the current. In all the water experiments, the robot was fitted with floating tanks at its bottom to ensure it did not sink in case of mechanical or electronic failure. However, along with all the experiments, the robot demonstrated high reliability without any technical failure.

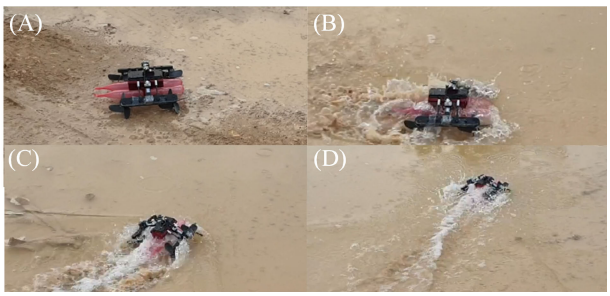

FIGURE 17. AmphiSTAR transitioning from crawling to swimming and then crawling (see video) [31].

It is noted that the current version swims at the water's surface only. In theory, the mechanism can also allow diving. However, diving underwater requires tethering or a relatively advanced autonomous guidance system which is unlikely to be fitted on a robot of this size.

VI. CONCLUSION

This paper presents a novel, highly mobile amphibious STAR robot (AmphiSTAR) that can crawl on the ground, swim, and hover on the water at high speeds. Compared to its size, the AmphiSTAR is the fastest amphibious robot to our knowledge, reaching 13.6 bodylengths/s on land and speeds of up to 5.6 bodylenghts/s in water. The lift forces elevate the robot above the water surface, which reduces friction, and its high-speed motors provide forward thrust, enabling it to move at very high speeds. The 3D printed 246 grams AmphiSTAR is a "wheeled" robot but draws its inspiration from cockroaches (for sprawling) and from the Basilisk lizard (for hovering on water).

We found that as the propeller increases its speed, it displaces the water beneath it, creating a vertical lift force. This effect becomes more visible at higher speeds (beyond 100 RPM) as the propeller ceases behaving like a fully submerged propeller as the water displacement becomes larger. Due to the water displacement, there is less effective area of the propeller in contact with the water, and the lift forces become smaller than a regular fully submerged propeller. The lift force as a function of rotational speed asymptotically converges to the force equivalent to the rotating volume of the propellers. For propellers with a constant blade angle and radii, the ratio of the displaced water to the total rotating volume is a function of the rotational speed alone. The ratio reaches 50%, 90%, and 95%, respectively, at speeds of 200, 620, and 1000 RPM.

We first measured the forces generated by propellers (30 and 45 degrees blade angles, 86 mm diameter). Across the full range of rotational speeds, 90% of the measured forces were within the error range of the experiments whereas the maximum errors were 16% and 19%, respectively for the 30 and 45 degrees blade. The errors can be attributed to measurement inaccuracies of the depth of the water at the beginning of the experiments, perturbations caused by waves flowing back from the basin's walls, and mutual turbulence from each propeller.

In general, the lift forces are composed of the water's lift force and the air's lift force. This was validated after measuring the lift coefficient and estimating the water level using the lift force equation. At 1000 RPM, the lift force caused by the air was nearly 2% of the total lift force. The value increased to 8% at 1500 RPM. In all the experiments, the measured forces were quite close to the theoretical expectations. The average deviation of the forces at 1000 RPM for different heights and sizes was 11.7%(maximum deviation 22%).

Finally, our modeling and experiments show that the robot has natural stability when hovering over the water in the yaw and roll directions. Our experiments indicate that the robot recovers from a 15 degrees perturbation in only 0.5 seconds and that tilting from centripetal acceleration at 1.5 m/s and the turning radius of 0.5 m were less than one degree.

Future research could include optimizing the design of the propellers and finding an optimal design in which the weight can be supported by the buoyancy while the forward thrust by the propellers.

REFERENCES

[1] J. M. Morrey, B. Larribrecht, A. D. Horchler, R. E. Ritzmann, and R. D. Quinn, "Highly mobile and robust small quadruped robots," in *Proc. IEEE/RSJ Int. Conf. Intell. Robots Syst. (IROS)*, 2003, pp. 82–87.
[2] P. Birkmeyer, K. Peterson, and R. S. Fearing, "DASH: A dynamic 16g hexapedal robot," in *Proc. IEEE/RSJ Int. Conf. Intell. Robots Syst.*, Oct. 2009, pp. 2683–2689.
[3] A. O. Pullin, N. J. Kohut, D. Zarrouk, and R. S. Fearing, "Dynamic turning of 13 cm robot comparing tail and differential drive," in *Proc. IEEE Int. Conf. Robot. Autom.*, May 2012, pp. 5086–5093.
[4] K. C. Galloway, G. C. Haynes, B. D. Ilhan, A. M. Johnson, R. Knopf, G. A. Lynch, B. N. Plotnick, M. White, and D. E. Koditschek, "X-RHex: A highly mobile hexapedal robot for sensorimotor tasks," Dept. Mech. Eng. Appl. Mech., Univ. Pennsylvania, Philadelphia, PA, USA, Tech. Rep., 2010.

[5] D. Zarrouk, A. Pullin, N. Kohut, and R. S. Fearing, "STAR, a sprawl tuned autonomous robot," in *Proc. IEEE Int. Conf. Robot. Autom.*, May 2013, pp. 20–25.
[6] D. Zarrouk and R. S. Fearing, "Controlled in-plane locomotion of a hexapod using a single actuator," *IEEE Trans. Robot.*, vol. 31, no. 1, pp. 157–167, Feb. 2015.
[7] D. Zarrouk and L. Yehezkel, "Rising STAR: A highly reconfigurable sprawl tuned robot," *IEEE Robot. Autom. Lett.*, vol. 3, no. 3, pp. 1888–1895, Jul. 2018.
[8] Y.-S. Kim, G.-P. Jung, H. Kim, K.-J. Cho, and C.-N. Chu, "Wheel transformer: A wheel-leg hybrid robot with passive transformable wheels," *IEEE Trans. Robot.*, vol. 30, no. 6, pp. 1487–1498, Dec. 2014.
[9] M. J. Spenko, G. C. Haynes, J. A. Saunders, M. R. Cutkosky, A. A. Rizzi, R. J. Full, and D. E. Koditschek, "Biologically inspired climbing with a hexapedal robot," *J. Field Robot.*, vol. 25, nos. 4–5, pp. 223–242, 2008.
[10] N. Tan, R. E. Mohan, and K. Elangovan, "Scorpio," *Int. J. Adv. Robotic Syst.*, vol. 13, no. 5, pp. 1–16, 2022.
[11] S.-C. Chen, K.-J. Huang, W.-H. Chen, S.-Y. Shen, C.-H. Li, and P.-C. Lin, "Quattroped: A leg–wheel transformable robot," *IEEE/ASME Trans. Mechatronics*, vol. 19, no. 2, pp. 730–742, Apr. 2014.
[12] Y. Sun and S. Ma, "Decoupled kinematic control of terrestrial locomotion for an ePaddle-based reconfigurable amphibious robot," in *Proc. IEEE Int. Conf. Robot. Autom.*, May 2011, pp. 1223–1228.
[13] S. Floyd and M. Sitti, "Design and development of the lifting and propulsion mechanism for a biologically inspired water runner robot," *IEEE Trans. Robot.*, vol. 24, no. 3, pp. 698–709, Jun. 2008.
[14] J. W. Glasheen and T. A. Mcmahon, "A hydrodynamic model of locomotion in the basilisk lizard," *Nature*, vol. 380, no. 6572, pp. 340–342, Mar. 1996.
[15] Y. Seong Song and M. Sitti, "Surface-tension-driven biologically inspired water strider robots: Theory and experiments," *IEEE Trans. Robot.*, vol. 23, no. 3, pp. 578–589, Jun. 2007.
[16] O. Ozcan, H. Wang, J. D. Taylor, and M. Sitti, "STRIDE II: A water strider-inspired miniature robot with circular footpads," *Int. J. Adv. Robotic Syst.*, vol. 11, no. 6, p. 85, Jun. 2014.
[17] Y. Chen, H. Wang, E. F. Helbling, N. T. Jafferis, R. Zufferey, A. Ong, K. Ma, N. Gravish, P. Chirarattananon, M. Kovac, and R. J. Wood, "A biologically inspired, flapping-wing, hybrid aerial-aquatic microrobot," *Sci. Robot.*, vol. 2, no. 11, Oct. 2017, Art. no. eaao5619.
[18] G. Chen, X. Ti, L. Shi, and H. Hu, "Design of beaver-like hind limb and analysis of two swimming gaits for underwater narrow space exploration," *J. Intell. Robotic Syst.*, vol. 104, no. 4, pp. 1–15, Apr. 2022.
[19] G. Chen, Y. Lu, X. Yang, and H. Hu, "Reinforcement learning control for the swimming motions of a beaver-like, single-legged robot based on biological inspiration," *Robot. Auto. Syst.*, vol. 154, Aug. 2022, Art. no. 104116.
[20] H. Xing, S. Guo, L. Shi, X. Hou, Y. Liu, H. Liu, Y. Hu, D. Xia, and Z. Li, "A novel small-scale turtle-inspired amphibious spherical robot," in *Proc. IEEE/RSJ Int. Conf. Intell. Robots Syst. (IROS)*, Nov. 2019, pp. 1702–1707.
[21] A. A. M. Faudzi, M. R. M. Razif, G. Endo, H. Nabae, and K. Suzumori, "Soft-amphibious robot using thin and soft Mckibben actuator," in *Proc. IEEE Int. Conf. Adv. Intell. Mechatronics (AIM)*, Jul. 2017, pp. 981–986.
[22] A. Crespi and A. J. Ijspeert, "Online optimization of swimming and crawling in an amphibious snake robot," *IEEE Trans. Robot.*, vol. 24, no. 1, pp. 75–87, Feb. 2008.
[23] A. Crespi, K. Karakasiliotis, A. Guignard, and A. J. Ijspeert, "Salamandra robotica II: An amphibious robot to study salamander-like swimming and walking gaits," *IEEE Trans. Robot.*, vol. 29, no. 2, pp. 308–320, Apr. 2013.
[24] D. Zarrouk, M. Mann, N. Degani, T. Yehuda, N. Jarbi, and A. Hess, "Single actuator wave-like robot (SAW): Design, modeling, and experiments," *Bioinspiration Biomimetics*, vol. 11, no. 4, Jul. 2016, Art. no. 046004.
[25] G. Dudek, P. Giguere, C. Prahacs, S. Saunderson, J. Sattar, L.-A. Torres-Mendez, M. Jenkin, A. German, A. Hogue, A. Ripsman, J. Zacher, E. Milios, H. Liu, P. Zhang, M. Buehler, and C. Georgiades, "AQUA: An amphibious autonomous robot," *Computer*, vol. 40, no. 1, pp. 46–53, Jan. 2007.
[26] Y. L. Young and B. R. Savander, "Numerical analysis of large-scale surface-piercing propellers," *Ocean Eng.*, vol. 38, no. 13, pp. 1368–1381, Sep. 2011.
[27] L. Schouveiler, F. S. Hover, and M. S. Triantafyllou, "Performance of flapping foil propulsion," *J. Fluids Struct.*, vol. 20, no. 7, pp. 949–959, Oct. 2005.
[28] E. Yari and H. Ghassemi, "The unsteady hydrodynamic characteristics of a partial submerged propeller via a RANS solver," *J. Mar. Eng. Technol.*, vol. 14, no. 3, pp. 111–123, Sep. 2015.
[29] K.-J. Paik, "Numerical study on the performance of a partially submerged propeller in bollard condition," in *Proc. 5th Int. Symp. Mar. Propulsors (SMP)*, vol. 11, 2017, pp. 723–730.
[30] O. Furuya, "A performance-prediction theory for partially submerged ventilated propellers," *J. Fluid Mech.*, vol. 151, pp. 311–335, Feb. 1985.
[31] A. Cohen and D. Zarrouk, "The AmphiSTAR high speed amphibious sprawl tuned robot: Design and experiments," in *Proc. IEEE/RSJ Int. Conf. Intell. Robots Syst. (IROS)*, Oct. 2020, pp. 6411–6418.
[32] N. Meiri and D. Zarrouk, "Flying STAR, a hybrid crawling and flying sprawl tuned robot," in *Proc. Int. Conf. Robot. Autom. (ICRA)*, May 2019, pp. 5302–5308.
[33] M. Rafeeq, S. F. Toha, S. Ahmad, and M. A. Razib, "Locomotion strategies for amphibious robots—A review," *IEEE Access*, vol. 9, pp. 26323–26342, 2021.
[34] X. Ma, G. Wang, and K. Liu, "Design and optimization of a multimode amphibious robot with propeller-leg," *IEEE Trans. Robot.*, vol. 38, no. 6, pp. 3807–3820, Dec. 2022.

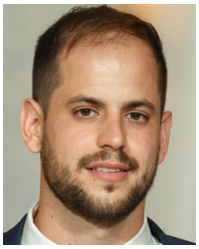

AVI COHEN received the B.Sc. and M.Sc. degrees from the Ben Gurion University of the Negev, Israel, in 2018 and 2020, respectively. He is currently pursuing the Ph.D. degree with the Bio-Inspired and Medical Robotics Laboratory, under the supervision of Dr. David Zarrouk and Dr. Avishay Sintov. His current research interests include designing redundant serial robots, control, navigation, and motion planning using a combination of heuristics and machine learning approaches. He received multiple excellence prizes for research and teaching.

DAVID ZARROUK received the B.Sc., M.Sc., and Ph.D. degrees from Technion, Israel, in 2005, 2008, and 2011, respectively.

From 2011 to 2013, he was a Postdoctoral Fellow with the Biomimetic Millisystems Laboratory, UC Berkeley. He is currently an Assistant Professor with the Department of Mechanical Engineering, Ben Gurion University of the Negev. His current research interests include medical robotics, robotics in flexible and slippery surfaces interactions, biomimetics, and minimally actuated mechanisms. He received multiple prizes for excellence in research and teaching, including the Fulbright Postdoctoral Fellowship, in 2011; the Fulbright-Ilan Ramon Postdoctoral Fellowship for most prominent Israeli Fulbright Fellow, in 2011; the best innovation awards of Surgical Robot Challenge in the Halymn International Symposium on Medical Robotics, in 2016, in the Israeli Conference on Mechanical Engineering, in 2017, and in the Israeli Conference on Robotics, in 2019; and the Best Paper Award in the 2019 IEEE RAL.